Blood-brain barrier-penetrative fluorescent anticancer agents triggering paraptosis and ferroptosis for glioblastoma therapy

Jiefei Wang[1,2], Mingyue Cao[3], Lulu Han[2], Ping Shangguan[2], Yisheng Liu[2], Yong Zhong[5], Chaoyue Chen[6], Gaoyang Wang[5], Xiaoyu Chen[2], Ming Lin[2], Mengya Lu[2], Zhengqun Luo[2], Mu He[2], Herman H. Y. Sung[6], Guangle Niu[1,3,*], Jacky W. Y. Lam[6], Bingyang Shi[2,*] & Ben Zhong Tang[4,6,*]

[1]School of Chemistry and Chemical Engineering, Beijing Institute of Technology, Beijing 100081, P. R. China
[2]Academy for Advanced Interdisciplinary Studies, Henan Key Laboratory of Brain Targeted Bio-nanomedicine, School of Life Sciences, Henan University, Kaifeng, Henan 475004, P. R. China
[3]State Key Laboratory of Crystal Materials, Shandong University, Jinan 250100, P. R. China
[4]School of Science and Engineering, Shenzhen Institute of Aggregate Science and Technology, The Chinese University of Hong Kong, Shenzhen (CUHK-Shenzhen), 518172, P. R. China
[5]Key Laboratory for Special Functional Materials of Ministry of Education, Henan University, Kaifeng 475004, P. R. China
[6]Department of Chemistry, Hong Kong Branch of Chinese National Engineering Research Center for Tissue Restoration and Reconstruction, State Key Laboratory of Molecular Neuroscience, Division of Life Science, Department of Chemical and Biological Engineering, The Hong Kong University of Science and Technology, Clear Water Bay, Kowloon, Hong Kong 999077, P. R. China

*Corresponding authors: niugl@bit.edu.cn (G. Niu); bs@henu.edu.cn (B. Shi); tangbenz@cuhk.edu.cn (B. Z. Tang)

Abstract

Currently used drugs for glioblastoma (GBM) treatments are ineffective, primarily due to the significant challenges posed by strong drug resistance, poor blood-brain barrier (BBB) permeability, and the lack of tumor specificity. Here, we report two cationic fluorescent anticancer agents (TriPEX-ClO_4 and TriPEX-PF_6) capable of BBB penetration for efficient GBM therapy via paraptosis and ferroptosis induction. These aggregation-induced emission (AIE)-active agents specifically target mitochondria, effectively triggering ATF4/JNK/Alix-regulated paraptosis and GPX4-mediated ferroptosis. Specifically, they rapidly induce substantial cytoplasmic vacuolation, accompanied by reactive oxygen species generation and intracellular Ca^{2+} overload, thereby disrupting metabolisms and inducing non-apoptotic cell death. In vivo imaging revealed that TriPEX-ClO_4 and TriPEX-PF_6 successfully traversed the BBB to target orthotopic glioma and initiated effective synergistic therapy post-intravenous injection. Our AIE drugs emerged as the pioneering paraptosis inducers against drug-resistant GBM, significantly extending survival up to 40 days compared to temozolomide (20 days) in drug-resistant GBM-bearing mice. These compelling results open up new venues for the development of fluorescent anticancer drugs and innovative treatments for brain diseases.

Glioblastoma (GBM), the most common and lethal central nervous system tumor, is characterized by its high invasiveness, rapid progression, and short median survival time of merely 14.6 months[1]. Unfortunately, the blood-brain barrier (BBB) shields the brain from almost all drugs[2, 3]. Temozolomide (TMZ) is the first-line chemotherapeutic drug for GBM[4, 5], functioning by inducing programmed cell apoptosis via aberrant DNA methylation[6]. However, GBM is refractory and highly resistant to TMZ treatment, primarily due to the presence of the DNA repair enzyme (O^6-methylguanine-DNA methyltransferase) in glioma cells, which allows GBM to evade apoptosis[7]. Alarmingly, more than 50% of patients treated with TMZ show no response, which, in combination with its low drug activity, results in a dismal prognosis[4]. Moreover, precise and effective drug development is dependent on guidance from previous in vivo studies and results from visual imaging analyses. However, current anticancer drugs lack high-sensitivity imaging capability and exhibit limited BBB penetration, low specificity, and inadequate drug efficacy[8]. This results in a scarcity of brain-targeting, highly specific drugs, which in turn impedes drug-resistant GBM theranostics.

Paraptosis is a newly identified programmed non-apoptotic cell death modality[9] that differs from other common forms of programmed cell death, such as apoptosis, autophagy, necroptosis, and pyroptosis[10]. It is characterized by prominent endoplasmic reticulum vacuolation and/or mitochondria swelling with disintegrated cristae[11-13]. In particular, mitochondria-targeting paraptosis inducers exhibit substantial potential to overcome therapeutic resistance in GBM by disrupting the energy supply of the intracellular "energy factory"[14, 15]. Certain natural compounds and metallic complexes, such as curcumin and celastrol could reportedly induce paraptosis-associated cell death[16-21]. Unfortunately, these drugs are associated with challenges such as poor BBB penetration, low drug activity, and insufficient mitochondrial targeting. Certain tumor-targeted metal-based (such as Cu- and Ir-based) nanodrugs were developed[22-25]. These nanodrugs not only efficiently

induced tumor paraptosis but also triggered other forms of cell death, such as Fe-, and Cu-induced ferroptosis[26-28], which resulted in an increased synergistic therapy. However, excessive overload of heavy metals can induce major organ dysfunction[29, 30] and has not been achieved in drug-resistant glioma due to poor mitochondrial targeting and BBB permeability[31]. Moreover, the lack of imaging capabilities of most drugs hinders in vivo study. Thus, the development of metal-free paraptosis drugs with high paraptosis activity and BBB-penetrating, mitochondria-targeting, and highly sensitive imaging capabilities holds tremendous promise and is a challenging task for effective therapy for drug-resistant glioma.

Aggregation-induced emission (AIE) is a unique photophysical phenomenon resulting in enhanced or boosted fluorescence in aggregate states[32-35]. The ingenious molecular design provides AIE luminogens (AIEgens) with distinct functions for in vivo biological imaging and disease theranostics, especially for brain disease treatment[36-42]. For example, we developed a positively charged therapeutic-type near-infrared (NIR) AIE probe (DNTPH). DNTPH, the first in vivo NIR theranostic agent, enables accurate real-time NIR imaging of BBB penetration and Aβ plaque detection. It facilitates Alzheimer's disease (AD) treatment by specifically binding and disassembling Aβ plaques to alleviate behavioral and cognitive deficits in AD mice[38]. Despite these advancements, there has been no report on the in vivo application of AIE-active anticancer agents capable of penetrating the BBB and targeting drug-resistant GBM for therapy. This is primarily due to the following challenges: (i) the need for optimization of molecules with suitable amphiphilicity, small molecular weight, and minimal steric hindrance to ensure high BBB permeability[43]; (ii) the preference for long wavelengths that penetrate deeply with high sensitivity, especially in the NIR window[44, 45]; however, constructing molecules by introducing strong donor/acceptor units or extending the π-conjugation process inevitably increases the molecular weight and impedes BBB penetration; (iii) high efficiency for activating paraptosis within specific organelles, particularly in the mitochondria, along with ensuring high biosafety[46]. Previously, Warner et al. reported that Rhodamine 6G-based fluorescent agents with specific counteranions selectively resulted in high cytotoxicity in cancer cells[47]. On the other hand, tetraphenylethylene is a highly suitable AIE building unit that has been studied extensively in diverse applications[48]. We hypothesized that incorporating the tetraphenylethylene unit into the skeleton of rhodamine derivatives could serve as an alternative approach to developing fluorescent anticancer drugs[49]. Building upon the concept of positively charged fluorescent probes for in vivo brain imaging[38, 41], the obtained cationic fluorescent compounds with balanced hydrophilic/lipophilic backbones could effectively cross the BBB for fluorescence visualization and drug-resistant GBM treatment.

Herein, we developed four cationic therapeutic AIEgens, named TriPEX-ClO_4, TriPEX-PF_6, TPEX-ClO_4, and TPEX-PF_6 based on tetraphenylethylene-fused and conjugated theranostic rhodamine analogs for TMZ-resistant GBM treatment (**Fig. 1**). Their photophysical properties were studied by performing fluorescence spectra analysis, density functional theory (DFT) calculations, and crystal packing analysis. The effects of steric hindrance and counteranions on the structure-activity relationship were investigated. Owing to their smaller steric hindrance, TriPEX-ClO_4 and TriPEX-PF_6 showed higher cell toxicity than TPEX-ClO_4 and TPEX-PF_6. These positively charged AIEgens could specifically target the mitochondria of tumor cells and induce paraptosis and ferroptosis. These compounds effectively targeted eleven tumor cell lines with higher specificity and universality over healthy cells, with particular efficacy against TMZ-resistant glioma (U251-TR) cells. Real-time fluorescence image monitoring and cellular protein analyses revealed that TriPEX-ClO_4 and TriPEX-PF_6 effectively triggered ATF4/JNK/Alix-regulated paraptosis, with concurrent weak activation of the GPX4-mediated ferroptosis pathway in U251-TR cells. Importantly, the balanced amphiphilicity of TriPEX-ClO_4 and TriPEX-PF_6 facilitated in vivo BBB penetration and specifically targeted the mitochondria of U251-TR cells to activate synergistic therapy against the orthotopic U251-TR tumor post intravenous injection. It led to a remarkable extension in the survival of U251-TR tumor-bearing mice from 18 days to 40 days, surpassing that of the TMZ-treated control group (20 days). Furthermore, the therapeutic efficacy and universality were also verified in subcutaneous HeLa-bearing mice. Overall, the development of the first BBB-penetrating, mitochondrial-targeting, red-emission anti-U251-TR AIE paraptosis drug, as a proof-of-concept, effectively resolves the challenge of the therapeutic resistance in GBM.

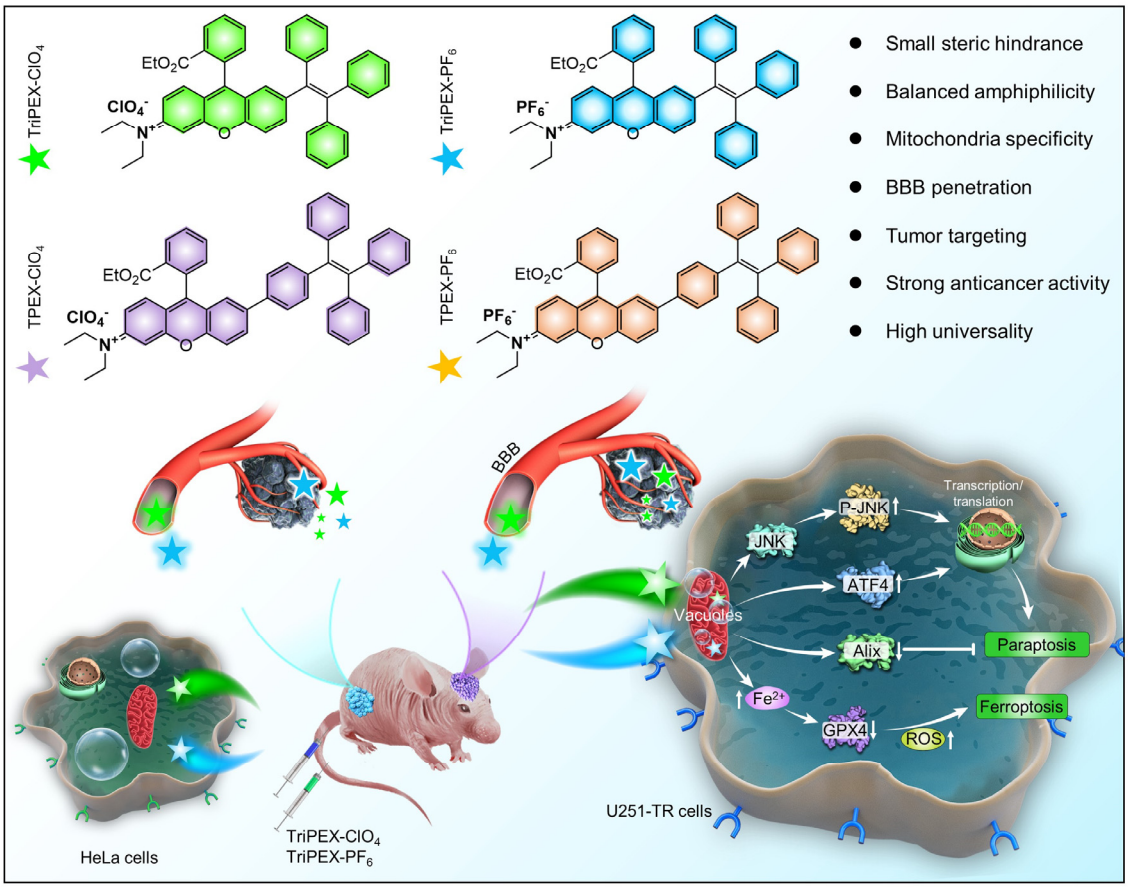

Fig. 1 | Schematic illustration for brain-targeted therapy using AIEgens. The upper section displays the chemical structures of AIEgens with various steric hindrances and coordination anions. The lower section displays the paraptosis pathway, along with the weak ferroptosis induced by TriPEX-ClO_4 and TriPEX-PF_6 against orthotopic TMZ-resistant glioma (U251-TR) and subcutaneous HeLa tumors.

Results

Structure characterization and optical properties of AIEgens

The synthesis pathways for cationic tetraphenylethylene-functionalized xanthene derivatives (TriPEX-ClO_4, TriPEX-PF_6, TPEX-ClO_4, and TPEX-PF_6) with different counteranions are depicted in **Supplementary Scheme 1**. The intermediates and final compounds were characterized by ^{1}H NMR, ^{13}C NMR, ^{19}F NMR, and HRMS spectroscopy (**Supplementary Figs. 1-23**). Moreover, the structures of TriPEX-ClO_4, TPEX-ClO_4, TPEX-PF_6, and a critical intermediate, c-TriPEX, were successfully confirmed using single crystal structure analysis (**Fig. 2a**, CCDC 1917199-1917202). The details of the X-ray experimental conditions, cell data, and refinement data are summarized in **Supplementary Tables 1-4**.

These compounds exhibited similar absorptions in DMSO, peaking at around 548 nm (**Supplementary Fig. 24**). Since tetraphenylethylene is a well-known rotor, they showed negligible fluorescence in DMSO (**Fig. 2b**), with fluorescence quantum yields (QYs) of less than 0.3% (**Supplementary Fig. 25**), due to strong non-irradiative transitions caused by free molecular motions. However, upon the addition of poorly soluble toluene to the DMSO solution, the red fluorescence intensity of these compounds increased slightly, and was then boosted with a toluene fraction ($f_{Toluene}$) of 90% (**Fig. 2b,c**), because of the formation of aggregates (**Supplementary Fig. 26**) and restriction of intramolecular motions[50]. These data confirmed that our synthesized molecules belonged to the AIEgen family. In addition, these AIEgens exhibited strong deep-red to NIR emissions (absolute QYs of up to near 7%) in the solid state (**Fig. 2d**). This significant enhancement in solid-state fluorescence can be attributed to the existence of multiple π−π, C−H···π, anion···π, C−H···O, and C−H···F interactions between adjacent molecules in the crystal state (**Supplementary Fig. 27**). Moreover, the boosted red fluorescence in viscous environments further validated the unique AIE characteristics of our molecules (**Supplementary Fig. 28**). Furthermore, DFT calculations revealed that the electrons of HOMOs were primarily delocalized on the tetraphenylethylene moiety, while those of LUMOs were mainly distributed across the xanthene skeleton (**Fig. 2e**). These typical electron separations and extended π-conjugations endow our donor-acceptor-structured AIEgens with long-wavelength fluorescence, with emissions extending to the NIR regions, which are advantageous for in vivo animal imaging.

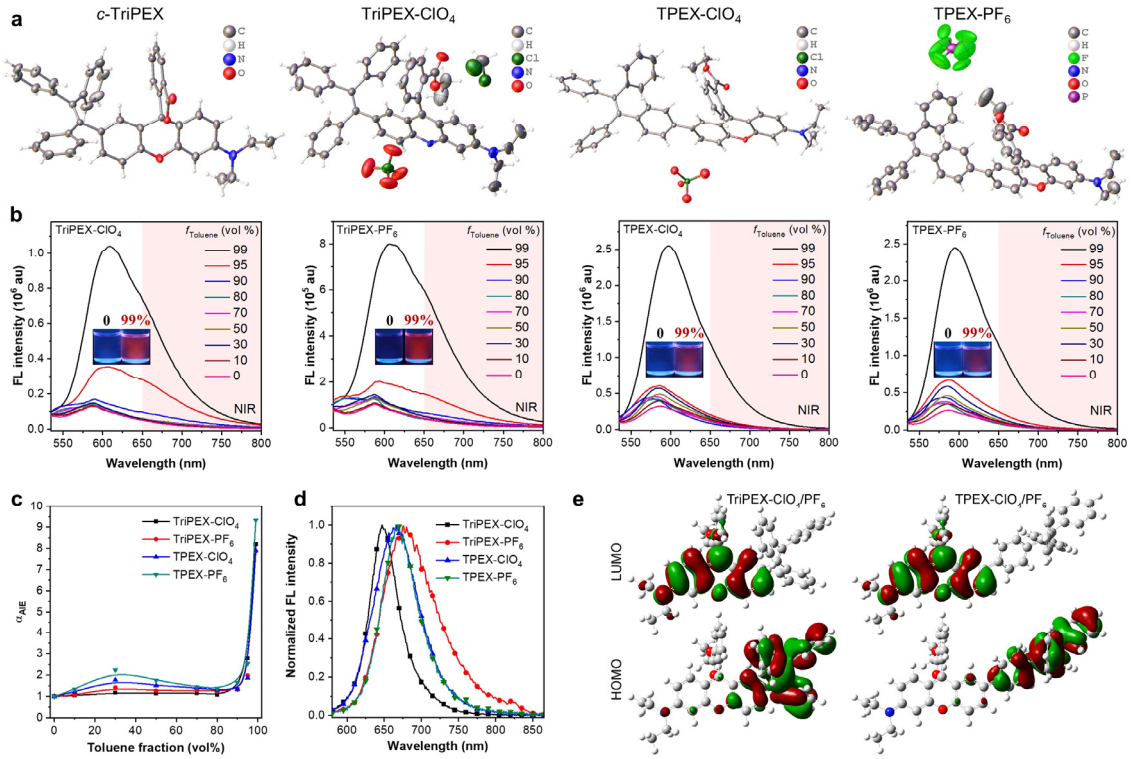

Fig. 2 | Crystal structures and optical properties of AIEgens. **a**, Single crystal X-ray structures of *c*-TriPEX, TriPEX-ClO_4, TPEX-ClO_4, and TPEX-PF_6. ORTEP drawing at the 50% probability level. **b**, Fluorescence (FL) spectra of the four AIEgens (10 μM) in DMSO and DMSO/toluene mixtures with different toluene fractions ($f_{Toluene}$). Inserts: Fluorescent photos of the four AIEgens (10 μM) in DMSO and DMSO/toluene mixtures, with 99% toluene fractions obtained under 365 nm UV irradiation using a hand-held UV lamp. **c**, Plots of α_{AIE} (fluorescence intensity I/I_0) versus the composition of the DMSO/toluene mixtures of the four AIEgens. **d**, Normalized fluorescence spectra of AIEgens in the solid state. **e**, Spatial electron distributions of the HOMOs and LUMOs of our AIEgens at optimized ground states at the B3LYP/6-31G (d,p) level.

Mitochondria-targeted highly selective toxicity to tumor cells

First, we evaluated the antitumor activity of four AIEgens in common HeLa and U251-TR cell lines to identify AIEgens (**Fig. 3a**). All AIEgens showed distinct concentration-dependent toxicity to HeLa cells and U25-TR cells. Remarkably, TriPEX-ClO_4 showed higher cell death rates of 78.9% (HeLa cells) and 78.6% (U25-TR cells) than those of TPEX-ClO_4 (52.2% and 35.4% for HeLa and U251-TR cells, respectively) at a concentration of 10 μM after incubation for 24 h. Similarly, TriPEX-PF_6 also showed higher cell death rates of 78.1% (HeLa cells) and 77.4% (U251-TR cells) than those of TPEX-PF_6 (52.3% and 31.3% for HeLa and U251-TR cells, respectively), indicating that the smaller steric hindrance led to higher anticancer activity but negligible impact from the counteranions. Subsequently, we selected TriPEX-ClO_4 and TriPEX-PF_6 as targeted molecules to investigate their mitochondria-targeting therapeutic mechanism. The targeting mitochondria in HeLa and U251-TR cells were tested via colocalization between the fluorescence of AIEgens and that of mitochondria-specific probe MitoTracker Green (MTG) under confocal laser scanning microscopy (CLSM). As depicted in **Fig. 3b**, the red fluorescence of AIEgens distinctly outlines the rounded and elongated mitochondria, and exhibits significant overlap with the green fluorescence of MTG, shown in yellow, demonstrating the superior mitochondria-targeting capability of TriPEX-ClO_4 and TriPEX-PF_6 in both tumor cell types.

Upon binding to mitochondria, the two AIEgens induced substantial levels of time-dependent cytoplasmic vacuolation (**Fig. 3c,d**), which is a characteristic morphological change associated with paraptosis[11-13]. Bio-transmission electron microscopy (Bio-TEM) was used to further identify whether the extensive vacuolization originated from the mitochondria or endoplasmic reticulum, and the results indicated a rapid and continuous mitochondrial swelling accompanied by disintegrated and disappearing cristae, without any notable cell membrane destruction that was characteristic of necrosis (**Fig. 3e,f**). The corresponding area of vacuolation in confocal and Bio-TEM images was quantified, as shown in **Fig. 3g,h**. The inverted-V inversion of vacuole number and increased vacuole volume collectively indicate mitochondrial fusion, dilation, and bursting upon exceeding a volume limitation. This process eventually leads to significant cell death, as visualized by the crystal violet images. All images revealed sparse residual HeLa or U251-TR cells treated with TriPEX-ClO_4 or TriPEX-PF_6, which suggested a high tumor cell death output (**Fig. 3i**). Moreover, high tumor specificity is crucial for anticancer drugs. Thus, we further investigated the cell toxicity of two AIEgens in two healthy cell lines (HA1800 and HT22 cells) and nine tumor cell lines, including glioma stem cells (X01 and 83) and A549 cells. As expected, TriPEX-ClO_4 and TriPEX-PF_6 exhibited highly selective cytotoxicity toward tumor cells but negligible toxicity to healthy cells (**Fig. 3j,k**), revealing their superior tumor-targeting capability, high biosafety,

and benign anticancer universality, which collectively demonstrated the significant potential of TriPEX-ClO_4 and TriPEX-PF_6 for treating drug-resistant glioma treatment through mitochondria-targeting paraptosis.

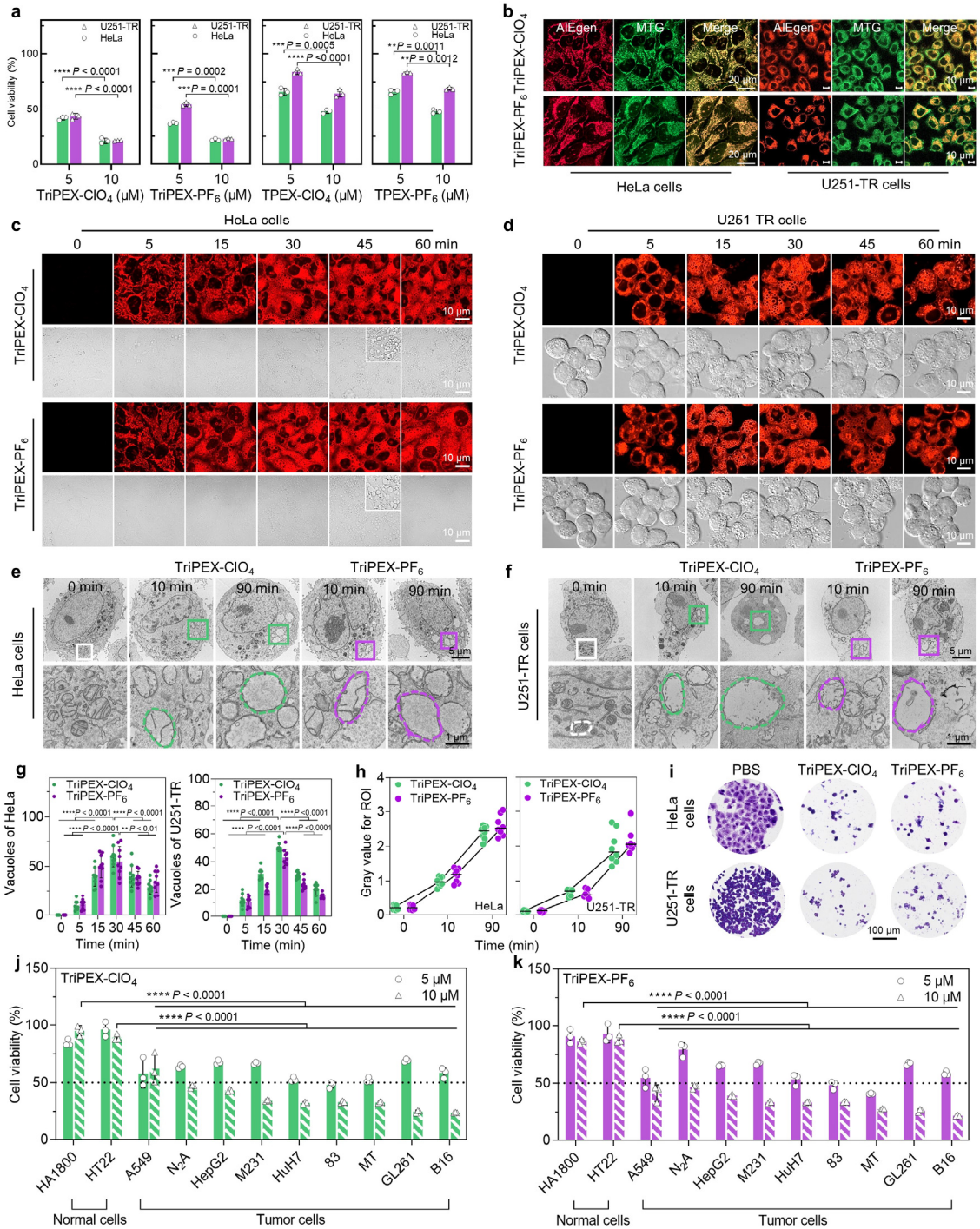

Fig. 3 | Mitochondria-targeted high-selectivity anticancer effect of AIEgens. a, Cell viability of four AIEgens in HeLa and U251-TR cells. **b**, Confocal images of HeLa and U251-TR cells incubated with TriPEX-ClO_4 (2 μM) and TriPEX-PF_6 (2 μM) and the MTG probe (200 nM). **c**,**d**, Confocal images of vacuoles in HeLa (**c**) and U251-TR (**d**) cells incubated with TriPEX-ClO_4 (6 μM) and TriPEX-PF_6 (6 μM) at various time points. **e**,**f**, Bio-TEM image showing a change in the vacuoles in HeLa (**e**) and U251-TR (**f**) cells incubated with TriPEX-ClO_4 (6 μM) and TriPEX-PF_6 (6 μM) as a function of time. **g**, Corresponding quantification of vacuole number in **c**,**d** as a function of time. **h**, Corresponding quantification of vacuole volume in **e**,**f** as a function of time. **i**, Photographs showing the proliferation of HeLa and U251-TR cells pre-treated with TriPEX-ClO_4 and TriPEX-PF_6 (6 μM) for 24 h and stained with crystal violet. **j**,**k**, Cell viability of healthy cells (HA1800 and HT22) and nine different tumor cells incubated with TriPEX-ClO_4 (6 μM) (**j**) and TriPEX-PF_6 (6 μM) (**k**) for 24 h. The data in **a**, **g**, **j**, and **k** are represented as mean ± SD values. *P* value is shown; all statistical analyses were compared via analyses of variance (ANOVA). NS, no significance, $^{**}P < 0.01$, $^{***}P < 0.001$, and $^{****}P < 0.0001$.

Unveiling the anticancer mechanism

Paraptosis, a type of programmed cell death, relies on protein synthesis processes necessitating transcription and translation. Paraptosis was mediated by positive signal transduction pathways of mitogen-activated protein kinase (MAPK), including c-Jun N-terminal kinase (JNK), extracellular signal-regulated kinase (ERK),

and p38[16, 22]. This cell death mode is also inhibited by the multifunctional adapter protein AIP-1/Alix[51, 52]. Moreover, paraptosis is often accompanied by an influx and overload of Ca^{2+}, redox homeostasis disruption, and metabolic imbalance[53]. To explore the underlying molecular mechanisms of cell death types other than paraptosis, we detected the viabilities of HeLa and U251-TR cells incubated with AIEgens and various inhibitors, including the apoptosis inhibitor (Z-DEVD-FMK, termed as DEVD), 3-methyladenine (3-MA, autophagy inhibitor), necrostatin-1 (Nec-1, necrosis inhibitor)[54, 55], and ferrostatin-1 (Fer-1, ferroptosis inhibitor). The toxicity results indicate negligible changes in viability other than an improvement in the Fer-1 treatment group (**Fig. 4a**; **Supplementary Fig. 29**), demonstrating that strong paraptosis was accompanied by weak ferroptosis, rather than other mechanisms.

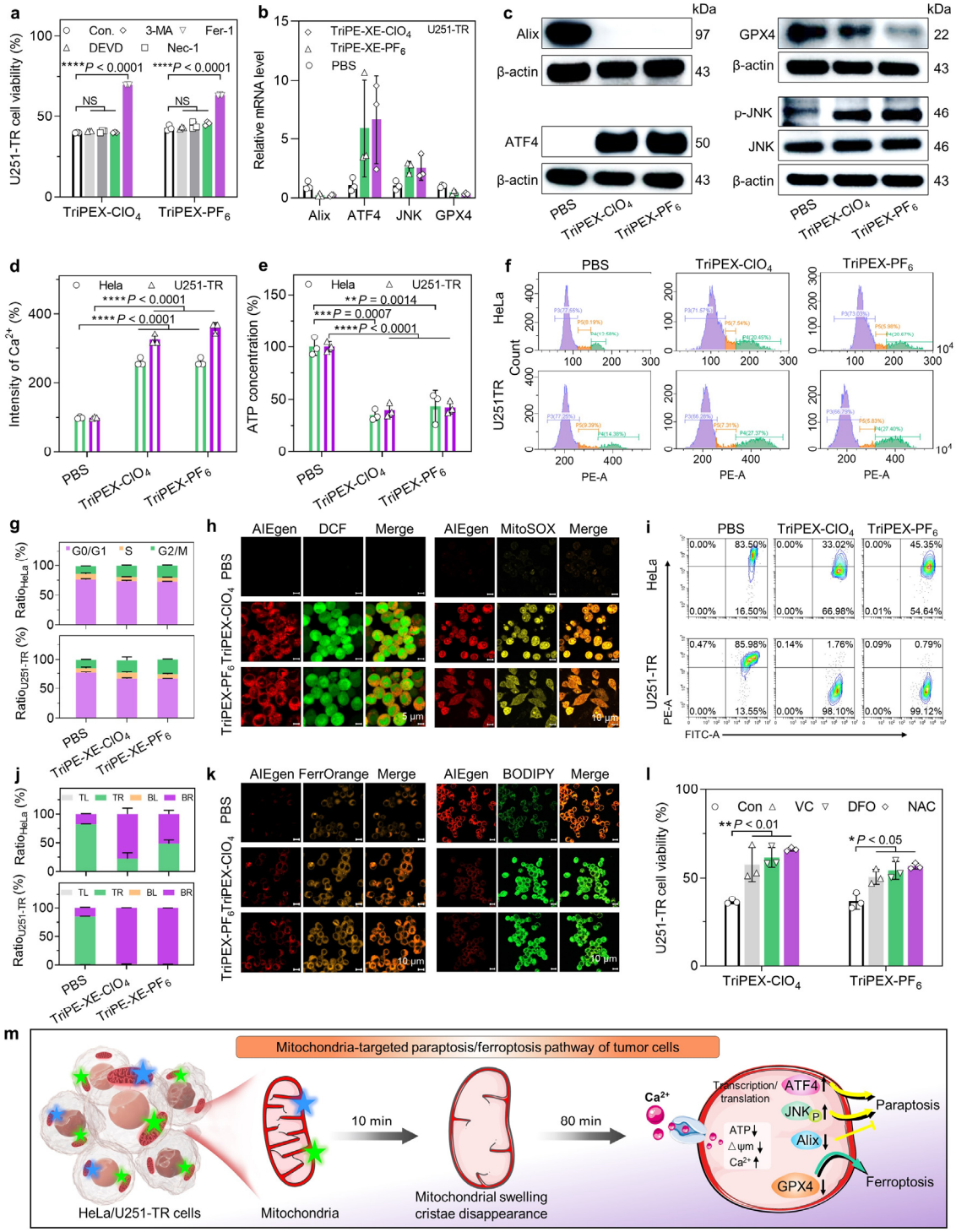

Fig. 4 | Mitochondria-targeting paraptosis and ferroptosis pathways induced by two AIEgens. a, Cell viabilities of U251-TR cells incubated with TriPEX-ClO_4 and TriPEX-PF_6 in the presence of DEVD, Nec-1, 3-MA, and Fer-1. **b**, Relative mRNA expression levels of Alix, ATF4, JNK, and GPX4 in U251-TR cells under various treatments (n = 3 independent samples). **c**, Western blot of Alix, ATF4, GPX4, p-JNK, and JNK proteins in U251-TR cells after treatments for 24 h. **d**,**e**, Intracellular calcium ion (Ca^{2+}) and ATP levels in U251-TR cells treated with two AIEgens. **f**,**g**, Cell cycle analysis and quantification of U251-TR cells under various treatments for 24 h via flow cytometry (n = 3 independent samples). **h**, Confocal images of ROS and mitochondrial superoxide in U251-TR cells treated with TriPEX-ClO_4 and TriPEX-PF_6 for 30

min and stained with DCFH-DA and MitoSOX probes. **i**,**j**, Flow cytometry analysis and quantification of changes in mitochondrial membrane potential in HeLa and U251-TR cells treated with PBS and two AIEgens for 4 h. Bottom left (BL), top right (TR), bottom right (BR), and top left (TL). **k**, Confocal images showing lipid peroxidation in U251-TR cells treated with two AIEgens for 30 min and FerroOrange or BODIPY 581/591 C11 probes. **l**, Cell viability of U251-TR cells incubated with two AIEgens in the presence of antioxidant ascorbic acid (VC), N-acetyl-L-cysteine (NAC), and ferroptosis inhibitors deferoxamine (DFO). **m**, Schematic illustration of mitochondria targeting paraptosis and ferroptosis pathways. Unless otherwise stated, the concentration and incubated time of two AIEgens were 6 μM and 24 h, respectively. The data in **a**, **b**, **d**, **e**, **g**, **j**, and **l** are represented as mean ± SD values. *P* value is shown; all statistical analyses were compared via analysis of variance (ANOVA). **P* < 0.05, ***P* < 0.01, ****P* < 0.001, *****P* < 0.0001, NS, no significance.

Subsequently, we used quantitative polymerase chain reaction (qRT-PCR) and western blot assays to examine the expression of key genes and proteins involved in paraptosis/ferroptosis synergistic pathways. As expected, the relative mRNA results (**Fig. 4b**; **Supplementary Fig. 30**) for two cell types showed decreased expression levels of ALG-2-interacting protein X (Alix) and glutathione peroxidase 4 (GPX4), along with increased levels of ATF4 and p-JNK (**Fig. 4c**; **Supplementary Fig. 31**). Meanwhile, protein levels of apoptosis-related p38 and p-p38, p-ERK, and ER-related Chop were assessed. The results showed that paraptosis is independent of apoptosis and has no apparent effect on ER and ERK-mediated MAPK pathways (**Supplementary Fig. 32**). Moreover, to further eliminate the possibility of apoptosis induction by these two AIEgens, a typical chemical therapy drug, doxorubicin (DOX), was used as the apoptosis control group. The Cleaved-Caspase-3 and Cleaved-PARP levels between DOX and our AIEgens were compared. The results indicated that DOX triggered high levels of apoptosis signals, while the two AIEgens only resulted in negligible changes (**Supplementary Fig. 33**). These data further confirmed that the cell death pathway involved is independent of the apoptosis mode.

As a result of the above pathways, the two AIEgens induced an extracellular calcium influx and intracellular calcium overload, resulting in phosphoric acid depletion, reduced ATP production, and disrupted metabolisms (**Fig. 4d,e**). Therefore, flow cytometry analysis and corresponding quantification revealed an increased proportion of cells in the gap 2 phase (G2-phase) / mitotic phase (M-phase) phase, with an average value of 22.3% in the TriPEX-ClO_4 group, 26.4% in the TriPEX-PF_6 group, and 14.4% in the PBS group, demonstrating effective cell cycle arrest (**Fig. 4f,g**). Ultimately, the process caused excessive oxidative stress, which was captured by 2'-7'dichlorofluorescin diacetate (DCFH-DA). As expected, the confocal imaging data in **Fig. 4h** and **Supplementary Fig. 34** demonstrated prominent ROS generation in HeLa and U251-TR cells treated with the two AIEgens, leading to a significant increase in mitochondrial superoxide levels, which were detected using Red Mitochondrial Superoxide Indicator (MitoSOX). Superoxide production resulted in a substantial decrease in mitochondrial membrane potential ($\Delta\Psi m$)[56], as evidenced by the distribution of cell spots in the top right (TR) quadrant gradually being transferred to the bottom right (BR) quadrant (**Fig. 4i,j**). Moreover, the proliferation of intracellular labile iron during ferroptosis was characterized via CLSM, and the results revealed bright yellow fluorescence signals from the FerrOrange probe in the two AIEgen-treated cell lines (**Fig. 4k**; **Supplementary Fig. 35**), implying a strong oxidation capability via the Fenton reaction. The combined oxidative stress from paraptosis and ferroptosis strongly induced lipid peroxidation, which was visualized by the intense green fluorescence captured by the BODIPY 581/591 C11 probe. The oxidation-induced damages in both cells could be markedly reversed with common reducing agents, including N-acetylcysteine (NAC), vitamin C (VC), and ferroptosis inhibitor deferoxamine (DFO)[57] (**Fig. 4l**; **Supplementary Fig. 36**). Taken together, TriPEX-ClO_4 and TriPEX-PF_6 triggered mitochondria-targeted cell death in HeLa and U251-TR cells through the ATF4/JNK/Alix-mediated paraptosis pathway and GPX4-guided ferroptosis pathway (**Fig. 4m**).

In vivo therapeutic effect assessment of the subcutaneous HeLa tumor model

The remarkable in vitro antitumor effects of TriPEX-ClO_4 and TriPEX-PF_6 prompted us to evaluate their therapeutic effects on common HeLa tumors in vivo. We first assessed their anticancer activity in the subcutaneous HeLa tumor-bearing mice model, following the therapy timeline depicted in **Fig. 5a**. The tumor-targeting capability of these AIEgens was monitored through fluorescence imaging. The highest fluorescence intensities of these AIEgens were observed at 4-6 h post-intravenous injection (**Fig. 5b**), corresponding to the most significant targeted accumulation in the tumor. After 5 cycles of tail intravenous injections (once every two days), evident tumor ablation and inhibited proliferation were observed in images obtained after hematoxylin-eosin (H&E) and Ki67 immunohistochemical analyses (**Fig. 5c**). Moreover, the down-regulation of Alix and GPX4, along with the up-regulation of ATF-4 and p-JNK confirmed that the paraptosis and ferroptosis mechanisms were consistent with in vitro results (**Fig. 5d**). Consequently, the synergistic paraptosis and ferroptosis processes induced by our AIEgens resulted in remarkable tumor inhibition (**Fig. 5e**), with only negligible weight loss (**Fig. 5f**). Furthermore, the H&E images of major organs in all groups exhibited no obvious pathological abnormalities or inflammation in cells (**Fig. 5g**), indicating the excellent biosafety of AIEgen treatments. Overall, these results demonstrated that TriPEX-ClO_4 and TriPEX-PF_6 are two safe and effective drugs against HeLa tumor through the synergistic pathways associated with paraptosis and ferroptosis.

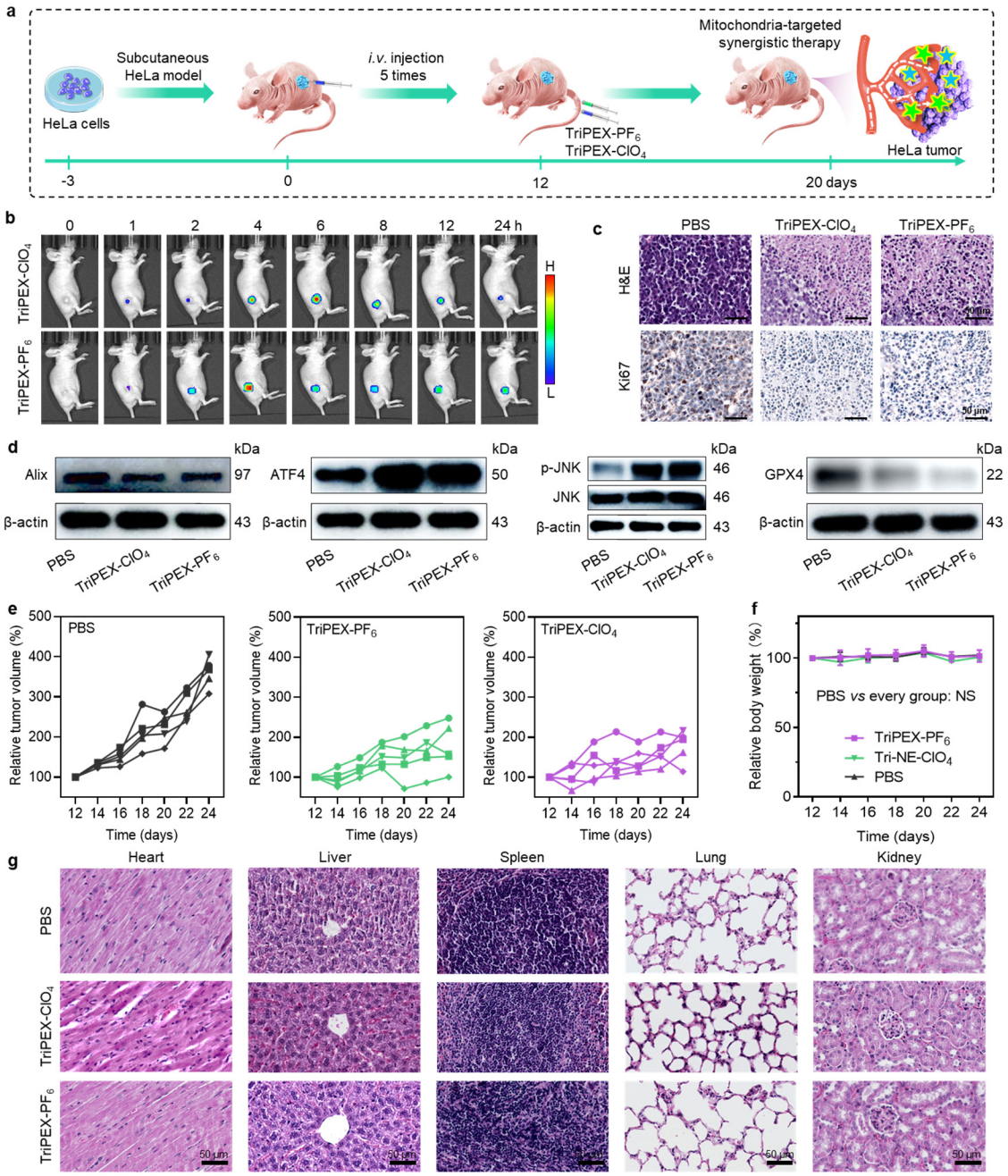

Fig. 5 | Therapeutic effects of TriPEX-ClO$_4$ and TriPEX-PF$_6$ on the subcutaneous HeLa tumor model. **a**, Therapy timelines of two AIEgens in the subcutaneous HeLa tumor model. **b**, In vivo fluorescence imaging of mice following the injection of two AIEgens (4.5 mg/kg). **c**, H&E and immunohistochemical of Ki67 of ex vivo tumor slices. **d**, Expression of paraptosis and ferroptosis-related proteins in ex vivo tumors. **e**, Relative tumor growth profiles throughout the therapy process (n = 5 independent samples). **f**, Relative body weight changes throughout the therapy process (n = 5 independent samples). **g**, H&E images for various organs of mice with various treatments. The data in **f** is represented in terms of mean ± SEM values. *P* value is shown; the statistical analysis results are compared using ANOVA. NS, no significance.

In vivo anticancer activity assessment in the orthotopic TMZ-resistant GBM model

In addition to common HeLa tumors, we further evaluated the in vivo therapy efficiency of TriPEX-ClO$_4$ and TriPEX-PF$_6$ in the TMZ-resistant GBM-bearing mouse model (U251-TR) using a pre-designed protocol (**Fig. 6a**). First, we used real-time in vivo fluorescence imaging to track the BBB penetration ability of the two molecules. The fluorescence intensities in the brain gradually increased over time with a maximum at 4 h post-injection (**Fig. 6b**), demonstrating the effective BBB-traversing ability of two AIEgens. The amphiphilicity of our AIEgens was estimated by calculated n-octanol/water partition coefficient (ClogP) values, estimated using the XlogP3 software[58]. TriPEX-ClO$_4$ and TriPEX-PF$_6$ showed a ClogP value of 7.03 for the positively charged skeleton, while TPEX-ClO$_4$ and TPEX-PF$_6$ had a ClogP value of 8.65, which further indicated that the balanced amphiphilicity of TriPEX-ClO$_4$ and TriPEX-PF$_6$ was beneficial for BBB penetration[59]. Moreover, the biodistribution of AIEgens in other main organs was investigated via fluorescence imaging (**Fig. 6c**). The quantitative analysis revealed that both AIEgens were significantly enriched in the liver and lungs (**Fig. 6d**). The accumulated AIEgens activated the synergistic pathways for effective U251-TR ablation, as assessed via

H&E staining observation of ex vivo brain slices after five times intravenous tail injections (administered once every two days). The glioma areas in the two treatment groups were significantly smaller than those in the PBS or TMZ control groups (**Fig. 6e**). Hence, an extended survival duration was observed in the TriPEX-ClO_4 group (40 days) and the TriPEX-PF_6 group (39 days) compared to that of the PBS group (18 days) and the TMZ-treated group (20 days), as shown in **Fig. 6f**. The negligible weight loss indicated high therapeutic safety (**Fig. 6g**). Furthermore, the detailed protein analyses of ex vivo gliomas indicated decreased expression levels of Alix and GPX4, and increased levels ATF4 and p-JNK (**Fig. 6h**), which is consistent with the in vitro results but different from that for the TMZ group. This confirms the activation of the in vivo paraptosis/ferroptosis pathways rather than the apoptosis pathway. The decreased expression of tumor vascular marker (CD31) and the increased expression of the cell death marker (TUNEL) in the two experimental groups proved the occurrence of angiogenesis disruption and effective tumor cell ablation because of ROS-induced vessel destruction and oxidative damage (**Fig. 6i**). The H&E images of main organs (**Supplementary Fig. 37**) and blood tests, including blood biochemical and routine blood tests, revealed no significant differences between the experimental groups and the PBS group, suggesting the excellent biocompatibility of our AIEgens (**Fig. 6j**). Collectively, these therapeutic results demonstrate the high specificity, BBB penetration capability, and effective antitumor activity and safety of these AIEgens against drug-resistant glioma.

Discussion

Resistance is a pervasive unresolved problem in cancer treatment that generally leads to treatment failures and high mortality rates, especially in individuals with challenging drug-resistant gliomas with minimal BBB permeability to standard drugs, such as TMZ. Paraptosis represents a new promising strategy for overcoming tumor cell resistance and improving cancer treatment efficacy. However, current paraptosis-inducing agents exhibit limited treatment efficacy and harmful side effects due to their their limited BBB permeability, poor tumor targeting capacity, and a lack of imaging functionality. Thus, the development of paraptosis agents for in vivo brain-targeted imaging and GBM treatment has remained unexplored. In this study, we successfully synthesized four cationic xanthene-based AIEgens, namely TriPEX-ClO_4, TriPEX-PF_6, TPEX-ClO_4, and TPEX-PF_6, with different tetraphenylethylene conjugation modes and counteranions to investigate their anticancer efficacy and BBB permeability. Among these AIEgens, TriPEX-ClO_4 and TriPEX-PF_6, with a relatively small level of steric hindrance, exhibited strong cytotoxicity specifically towards cancer cells over healthy cells. These two AIEgens specifically targeted the mitochondria, efficiently triggering ATF4/JNK/Alix-involving paraptosis and GPX4-mediated ferroptosis pathways. Specifically, they rapidly induced massive cytoplasmic vacuolation, reactive oxygen species generation, and intracellular Ca^{2+} overload, leading to disrupted metabolisms and eventual cell death. Significantly, the balanced amphiphilicity of TriPEX-ClO_4 and TriPEX-PF_6 enhanced their BBB permeability, enabling high-efficacy treatment of GBM through synergetic paraptosis and ferroptosis pathways. This unique treatment approach led to a remarkable extension of survival time of up to 40 days for U251-TR tumor-bearing mice compared to the TMZ-treated group (20 days). This work not only opens up new venues for the diagnosis and efficient therapy of drug-resistant orthotopic GBM, but also provides valuable insights into designing and synthesizing superior paraptosis-inducing anticancer drugs. Our fluorescent activators have tremendous potential in fundamental and clinical disease theranostic applications developed in the future for the induction of synergetic paraptosis and ferroptosis.

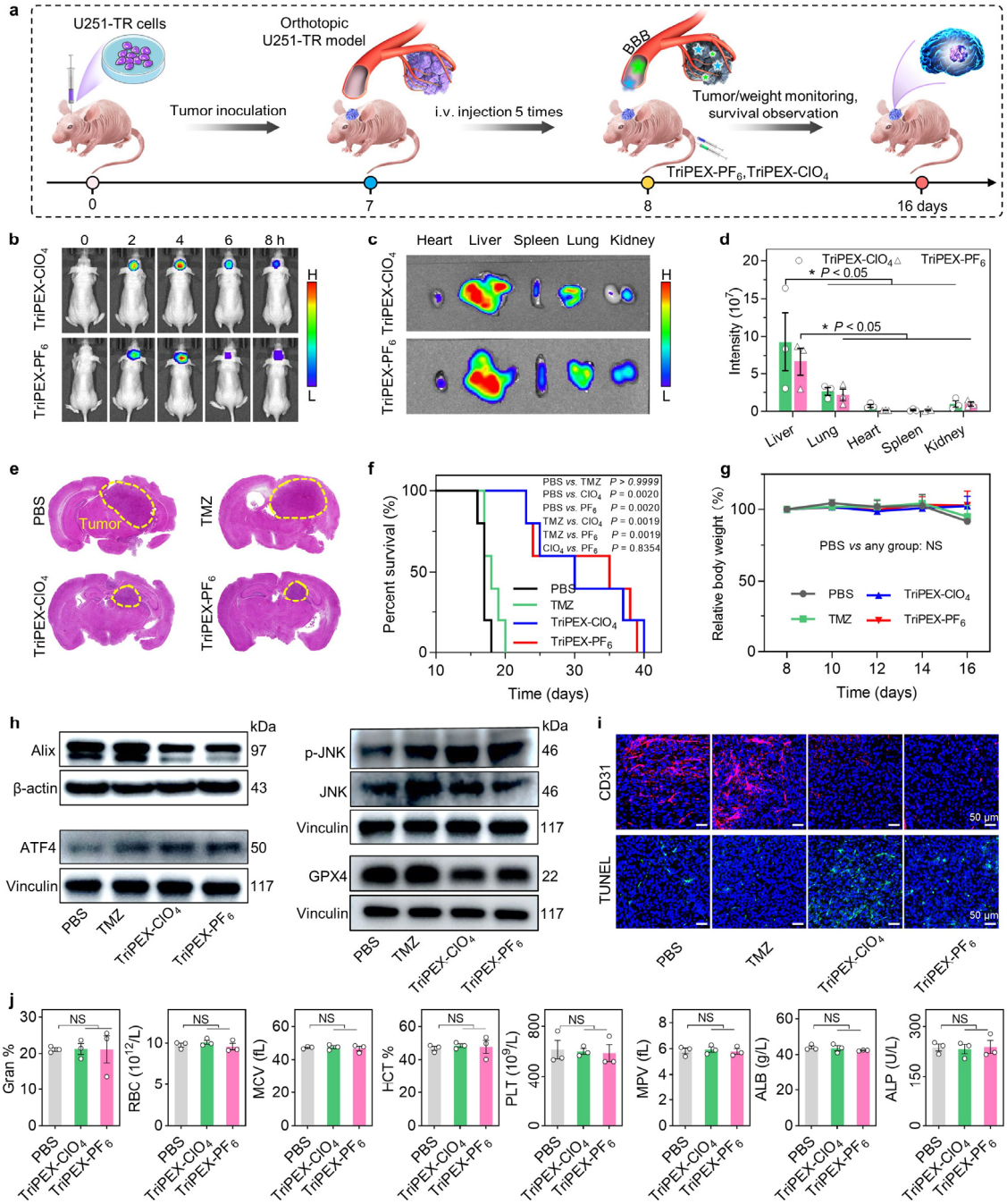

Fig. 6 | Therapeutic effects of TriPEX-ClO_4 and TriPEX-PF_6 on the orthotopic TMZ-resistant glioma model. **a**, Schematic illustration of the establishment of the U251-TR GBM orthotopic model and therapy timelines of the two AIEgens. **b**, In vivo fluorescence imaging in mice following the injection of TriPEX-ClO_4 and TriPEX-PF_6 (dosage: 4.5 mg/kg). **c**,**d**, Fluorescence images and quantification of biodistribution of two AIEgens in major organs. **e**, Images of H&E staining of ex vivo brain slices from various groups; the glioma area was marked by yellow lines. **f**,**g**, Survival (**f**) and body weight (**g**) monitoring of the U251-TR mice during the therapy process (n = 5 independent samples). **h**, Expression levels of various proteins in ex vivo gliomas post-treatment. **i**, Immunofluorescence images of CD31 and TUNEL images of ex vivo brain slices. **j**, Comparison of blood parameter values between healthy mice and two treatment groups (n = 3 independent samples). The data in **d** and **j** are represented as mean ± SEM values, **g** is the mean ± SD value. *P* value shown, all statistical analyses were compared via ANOVA tests. NS, no significance. $^*P < 0.05$.

Methods

Materials. All chemicals and biological reagents were purchased and used without further purification. The intermediate compounds **4** and **5** were purchased from AIEgen Biotech Co. 2',7'-dichlorodihydrofluorescein diacetate (DCFH-DA), Mitochondria-Tracker Green (MTG), Adenosine triphosphate (ATP) test kit, Fluo-4 calcium ion detection kit and Hoechst 33342 were obtained from Beyotime Biotechnology Co., Ltd. (Shanghai). The FerroOrange (Fe^{2+} probe) was purchased from Dojindo (Japan). The BODIPY 581/591 C11 (lipid peroxidation probe) was purchased from Thermo Fisher Scientific. The MitoSOX Red Mitochondrial Superoxide Indicator was bought from Yeasen Biotechnology Co., Ltd. (Shanghai). The Alix, ATF4 antibodies, and goat anti-rabbit IgG H&L (Alexa fluor® 488) were purchased from Abcam. The Caspase3, cleaved Caspase3, PARP, and Chop antibodies were obtained from Cell Signaling Technology, Inc. The JNK, phospho-JNK (p-JNK), p38, phospho-p38 (p-p38), ERK, phospho-ERK (p-ERK), and Ki67 were purchased from Beyotime

Biotechnology Co., Ltd. (Shanghai). The ACTB (β-actin) and the second antibody (goat anti-rabbit IgG, goat anti-mouse IgG) were obtained from Abclonal Technology Co., ltd. The necrostatin-1 (Nec-1), 3-methyladenine (3-MA), and deferoxamine (DFO) were purchased from Sigma-Aldrich. Ascorbic acid (VC) and N-acetyl-L-cysteine (NAC) were obtained from Aladdin Chemistry Co., Ltd. (Shanghai, China). The Z-D (OMe) E (OMe) VD (OMe)-FMK (Z-DEVD-FMK, DEVD) were bought from Abcam. The immunohistochemical kit was bought from Boster Biological Technology Co., Ltd. All antibodies were used following the manufacturer's instructions. All aqueous solutions were prepared using ultra-pure water with a resistivity of 18.2 MΩ cm. All air- and water-sensitive syntheses were carried out in flame-dried glassware in a nitrogen atmosphere.

Apparatus. The morphology of nanocomposites and fibrils was examined by a transmission electron microscopy (JEOL JEM-2100) device operating at an acceleration voltage of 200 kV. The size analysis was tested on a dynamic light scattering spectrometer (Malvern Nano ZS). UV-vis spectra were recorded on a Cary 3500 spectrophotometer. Fluorescence measurements were recorded on a FluoroLog-3 fluorescence spectrophotometer (Horiba-Jobin Yvon, France). NIR animal imaging was performed on a self-built imaging system with a NIRvana640 InGaAs camera. The in vivo ROS generation was monitored using the IVIS Spectrum animal imaging system (PerkinElmer, IVIS Lumina III). The cellular fluorescence microscopy images were observed by a confocal laser scanning microscope (Zeiss 880). The optical density of cell samples was examined on a multifunction microplate reader (Devices/13x). ^{1}H and ^{13}C spectra were measured on a Bruker AVIII 400 MHz NMR spectrometer using tetramethylsilane (TMS; $\delta = 0$) as an internal reference. The high-resolution mass spectra (HRMS) were recorded on a GCT Premier CAB048 mass spectrometer system operating in a MALDI-TOF mode.

Synthesis of four AIEgens. The detailed synthesis procedure and route of four AIE molecules are shown in the Supporting Information.

Cell culture. The HeLa and trimetazidine (TMZ)-resistant U251 (U251-TR) cells were used for in vitro experiments and the establishment of the subcutaneous HeLa tumor and orthotopic glioma model. The HeLa and U251-TR cells were cultured in Dulbecco's Modified Eagle's medium (DMEM) containing 10 % fetal bovine serum (FBS), 10 U/mL penicillin, and 10 mg/mL streptomycin. The cells were incubated at 37 ℃ in a humidified atmosphere containing 5 % CO_2.

In vitro antitumor studies. The cytotoxicity assay kit (CCK-8) was used to evaluate the cytotoxicity. The HA1800, HT22, HeLa, U251-TR, GL261, A549, N2A, B16, HuH7, HepG2, M231, MT, and 83 cells were plated in 96-well plates (all were 5×10^3 cells per well) and further grow for 24 h. Then the mediums were replaced with fresh medium containing different concentrations (5 and 10 μM) of TriPEX-PF_6 and TriPEX-ClO_4, respectively, for 24 h. Subsequently, the cells were washed three times with PBS and incubated with the CCK8 solution (10 μL per well) for 1 h. The optical density at 450 nm was measured in a microplate reader (Devivces/13x). The toxicity of HeLa cell and U251-TR cells treated with TPEX-PF_6 (6 μM) and TPEX-ClO_4 (6 μM) also were evaluated following the above procedures. The cytotoxicity-inhibited assays were performed according to the same procedure except for the co-incubation of TriPEX-PF_6 (6 μM) or TriPEX-ClO_4 (6 μM) combined with various inhibitors for 24 h. The detailed concentrations of various inhibitors were DEVD (100 μM), Nec-1 (50 μM), 3-MA (100 μM), DFO (400 μM), VC (2 mM), and NAC (5 mM).

Crystal violet assay. HeLa and U251-TR cells were inoculated in 12-well plates (1.5×10^5 cells per well) and allowed to culture for 24 h. Afterward, the culture medium was replaced by fresh medium containing PBS, TriPEX-PF_6 (6 μM), and TriPEX-ClO_4 (6 μM), respectively, for another 24 h. Then the culture medium was removed and washed with PBS. 500 μL of polyformaldehyde fixing solution was added to the well. Subsequently, the cells were fixed for 20 min at room temperature. After fixing, the cells were washed with PBS and incubated with the crystal violet staining solution (500 μL per well) for 30 min at room temperature. Subsequently, the cells were washed with PBS until no obvious purple color was observed, and the pictures were finally taken with an inverted fluorescence microscope.

In vitro confocal imaging. Mitochondrial co-localization, intracellular reactive oxygen species (ROS), mitochondrial superoxide levels, labile iron (Fe^{2+}), and lipid peroxidation levels were monitored by confocal imaging with Mito-Tracker Green (MTG), DCFH-DA, Mito-SOX, FerroOrange, and BODIPY 581/591 C11 probes, respectively. 1 mL of HeLa and U251-TR cells (1×10^5 cells/well) were seeded in a glass bottom dish for 24 h and then incubated with 500 μL fresh medium containing TriPEX-PF_6 (6 μM) or TriPEX-ClO_4 (6 μM) for 30 min. After washing three times with PBS, the cells were co-stained by the above five probes according to the specifications. All dishes were sent to the confocal laser scanning microscope (CLSM, Zeiss 880) observation.

Mitochondrial membrane potential test. Mitochondrial membrane potential was monitored by flow cytometry using the JC-1 probe. HeLa and U251-TR cells were inoculated in 6-well plates (2×10^5 cells per well) and cultured for 24 h. The culture medium was replaced by a fresh medium containing PBS, TriPEX-PF_6 (6 μM), and TriPEX-ClO_4 (6 μM), respectively, for 4 h. After washing three times with PBS, the cells were stained by the JC-1 probe according to the specification and sent for flow cytometry analysis.

Detection of intracellular Ca^{2+} concentration. The Fluo-4AM calcium probe was used to detect the intracellular calcium (Ca^{2+}) concentration. HeLa and U251-TR cells were seeded in 6-well plates (5×10^4 cells per well) and cultured for 24 h. Then, the culture medium was replaced by fresh medium containing PBS, TriPEX-PF_6 (6 μM), and TriPEX-ClO_4 (6 μM), respectively, for 24 h. After washing three times with PBS, the cells were stained by the Fluo-4AM probe according to the specification. All dishes were directly sent to the microplate reader (Devivces/13x) for further analysis.

ATP level detection. An ATP kit was used to assess the cellular ATP levels. HeLa and U251-TR cells were seeded in 12-well plates (1.5×10^5 cells per well) and cultured for 24 h. Then the culture medium was replaced by fresh medium containing PBS, TriPEX-PF_6 (6 μM), and TriPEX-ClO_4 (6 μM), respectively, for 24 h. The cells were lysed with 200 μL of

lysate and centrifuged at 12000 g for 5 min under 4 ℃. The resulting supernatant was diluted 10 times for subsequent determination. According to the instructions, The ATP detection solution was prepared and added to the 96-well plate after eliminating the background of ATP in advance. Subsequently, 20 μL of the diluted samples were added to each hole and further incubated for 10 min. Finally, the luminescence detection was carried out by a microplate reader to quantify the ATP levels of two cells.

Cell cycle test. Firstly, HeLa and U251-TR cells (2×10^5 cells per well) were inoculated in 6-well plates and cultured for 24 h. Then, the culture medium was replaced with a serum-free culture medium. After 12 h of starvation, the cells were treated with PBS, TriPEX-PF_6 (6 μM), and TriPEX-ClO_4 (6 μM), respectively, for 24 h. Subsequently, the digested cell suspension was dropped into 80 % pre-cooled ethanol and fixed overnight at -20 ℃. Subsequently, the cells were centrifuged and suspended in PBS. 10 μg of RNase was added to the cell suspension and incubated at 37 ℃ for 30 minutes. Then, the cell suspensions were stained with propidium iodide (PI) for 30 min in the dark at room temperature. Finally, the stained cell suspensions were analyzed using a flow cytometry test.

Western blotting test. HeLa and U251-TR cells (2×10^5 cells per well) were seeded in 6-well plates and cultured for 24 h. The cells were treated with PBS, TriPEX-PF_6 (6 μM), and TriPEX-ClO_4 (6 μM), respectively, for another 24 h. Then the cells were lysed in 0.1 mL RIPA buffer containing protease and phosphatase inhibitors. After that, the protein concentration of all samples was quantified using a BCA kit. The proteins were separated on 10 % SDS-PAGE, then transferred to a polyvinylidene fluoride (PVDF) membrane, and sealed with 5% skim milk for 1 h at room temperature. The membranes were incubated with corresponding primary antibodies including ACTB (β-actin, 1:5000), PARP (1:1000), Caspase3 (1:1000), cleaved-Caspase3 (1:1000), GPX4 (1:1000), Alix (1:5000), ATF4 (1:1000), Chop (1:1000), JNK (1:1000), phospho-JNK (p-JNK, 1:1000), p38 (1:1000), phospho-p38 (p-p38, 1:1000), ERK (1:1000), phospho-ERK (p-ERK, 1:1000) at 4 ℃ overnight. Subsequently, the membranes were incubated with a second antibody (goat anti-rabbit IgG, goat anti-mouse IgG,1:5000 dilution) at 25 ℃ for 1 h, followed by washing with TBST three times. Finally, the membranes were observed using ECL imaging observation with Super Signal ECL (Pierce). The protein analysis of tumor tissue followed the same procedures, except that tissue samples were collected after the completion of in vivo treatment.

RNA extraction and quantification. HeLa and U251-TR cells (2×10^5 cells per well) were cultured in 6-well plates for 24 h. Then the cells were treated with PBS, TriPEX-PF_6 (6 μM), and TriPEX-ClO_4 (6 μM), respectively, for another 24 h. The total RNA was extracted from the two cells using RNAprep FastPure tissue cell kit (Tsingke Biotechnology Co., Ltd.), following the manufacturer's instructions. The total RNA (1 μg) was used as a template and synthesized by PrimeScrip RT Master Mix (Takara). LightCycler 480 Ⅱ real-time detection system (Roche) was used for PCR analysis. The level the target gene were normalized to GAPDH expression. Details of the primers are shown in Supplementary Table 5.

Establishment of two tumor models. The animal experiments were approved by the Medical and Scientific Research Ethics Committee of Henan University School of Medicine (PR China) (HUSOM-2022-336). Balb/c nude mice (female, 6-8 weeks) were purchased from SiPeiFu (Beijing) Biotechnology Co., Ltd. All mice were housed in a 12-h dark/light cycle and maintained at an ambient temperature (24 ℃), and with 50% humidity. For the U251-TR tumor-bearing mice model, the U251-TR cell suspension (2×10^3) in 5 μL of 0.9% NaCl was implanted into the left striatum of mice. Then the pores were sealed with bone wax and tissue glue. On the seventh day, the model is considered to be successfully established when the mice have enough bioluminescence intensity. For the subcutaneous HeLa tumor-bearing model, the HeLa cells (6×10^6) in 0.9% NaCl were inoculated subcutaneously in the thigh root of nude mice. Once the tumor volume reaches about 100 mm^3, the tumor model is considered to be successfully established.

In vivo therapeutic assessment. The HeLa tumor-bearing mice were randomly divided into three groups: PBS group, TriPEX-PF_6 group, and TriPEX-ClO_4 group. The orthotopic U251-TR tumor-bearing mice were randomly divided into four groups: PBS, TMZ, TriPEX-PF_6, and TriPEX-ClO_4 groups. The corresponding specimens were intravenously injected (TriPEX-PF_6 and TriPEX-ClO_4 dosage: 4.5 mg/kg, TMZ dosage: 2.5 mg/kg) once every 2 days for a total of 5 treatments. The tumor length and width of HeLa tumor-bearing mice were recorded by a vernier caliper. The body weight change of the two models and the survival time of U251-TR tumor-bearing mice were recorded during the therapy process. After treatment, the main organs (heart, liver, spleen, lung, and kidney) and tumor or brain tissues of the mice were stained with hematoxylin and eosin (H&E). The protein in the tumor tissue was homogenized in the lysate at 0.2 mL at 4 ℃ for 30 min. The supernatant was centrifuged at 15000 rpm for 30 min, and the obtained samples were sent to the western blot analyses.

Immunocytochemistry analysis. After finishing the tumor treatment experiment, the tumors of subcutaneous HeLa tumor-bearing mice and the brains of the U251-TR glioma-bearing mice were collected and prepared into slices after the fixation, immersion, slicing, and serum-blocking processes. Subsequently, the slices were stained with a Ki67 immunohistochemical kit (Boster Biological Technology Co., Ltd.) according to the instructions, and followed by hematoxylin staining. Finally, the image collection and analyses of these slices were performed using a slide scanner (Grundium OCUS40X).

Immunofluorescence analysis. After the tumor treatment experiment, the mice were sacrificed. The tumors of subcutaneous HeLa tumor-bearing mice and the brains of the U251-TR glioma-bearing mice were collected and then prepared into slices after the fixation, immersion, slicing, and serum-blocking processes. These slices were stained with a TUNEL apoptosis detection kit according to the instructions. Additionally, some sections were stained with the first antibody CD31 and the Goat Anti-Rabbit IgG H&L (Alexa Fluor® 488, 488-labeling secondary antibodies). Lastly, the slices were sent to the confocal laser scanning microscope (Zeiss 880) observation after staining with nucleus dye (Hoechst).

Blood biochemistry and blood routine examination. Healthy Balb/c mice were randomly divided into three groups: PBS, TriPEX-PF_6, and TriPEX-ClO_4 groups, with a dosage of 4.5 mg/kg administered via *I.V.* tail injection. Blood samples (100

μL) were collected from the tails of mice on the 10th day after injection. Standard blood chemical parameters were analyzed with an automated chemical analysis analyzer (Chemray 240 Rayto Inc.) with a kit from Wuhan Servicebio Technology Co. Ltd. Additionally, an automated blood cell analyzer (BC-2800Vet-Mindray Inc.) was used for blood cell parameter analysis.

Statistical analysis. All results were presented as mean ± standard deviation (SD) or means ± standard error of the mean (SEM) based on at least three independent experiments. Statistical analysis among multiple datasets was compared by analysis of variance (ANOVA), while that in two-dataset experiments was compared using a two-tailed Student's t-test in GraphPad Prism 8.0. *P* values < 0.05 were considered statistically significant, denoted as $*P < 0.05$, $**P < 0.01$ $***P < 0.001$, and $****P < 0.0001$. The survival curve was compared using the log-rank (Mantel-Cox) test.

Reporting summary. Further information on research design is available in the Nature Research Reporting Summary linked to this article.

Data availability

The main data supporting the results in this study are available within the paper and its Supplementary Information. The raw and analysed datasets generated during the study are too large to be publicly shared, yet they are available for research purposes from the corresponding author on reasonable request. Source data are provided with this paper.

References

1. Wen, P.Y. & Kesari, S. Malignant Gliomas in Adults. *N. Engl. J. Med.* **359**, 492-507 (2008).
2. Kim, T. *et al.* Deep brain stimulation by blood–brain-barrier-crossing piezoelectric nanoparticles generating current and nitric oxide under focused ultrasound. *Nat. Biomed. Eng.* **7**, 149-163 (2023).
3. Zhao, Z., Nelson, A.R., Betsholtz, C. & Zlokovic, B.V. Establishment and Dysfunction of the Blood-Brain Barrier. *Cell* **163**, 1064-1078 (2015).
4. Lee, S.Y. Temozolomide resistance in glioblastoma multiforme. *Genes Dis.* **3**, 198-210 (2016).
5. Stupp, R. *et al.* Radiotherapy plus Concomitant and Adjuvant Temozolomide for Glioblastoma. *N. Engl. J. Med.* **352**, 987-996 (2005).
6. Esteller, M. *et al.* Inactivation of the DNA-Repair Gene MGMT and the Clinical Response of Gliomas to Alkylating Agents. *N. Engl. J. Med.* **343**, 1350-1354 (2000).
7. Gong, L. *et al.* Characterization of EGFR-reprogrammable temozolomide-resistant cells in a model of glioblastoma. *Cell Death Discovery* **8**, 438 (2022).
8. van Solinge, T.S., Nieland, L., Chiocca, E.A. & Broekman, M.L.D. Advances in local therapy for glioblastoma — taking the fight to the tumour. *Nat. Rev. Neurol.* **18**, 221-236 (2022).
9. Sperandio, S., de Belle, I. & Bredesen, D.E. An alternative, nonapoptotic form of programmed cell death. *Proc. Natl. Acad. Sci. U.S.A.* **97**, 14376-14381 (2000).
10. Fuchs, Y. & Steller, H. Programmed Cell Death in Animal Development and Disease. *Cell* **147**, 742-758 (2011).
11. Xu, C.-c. *et al.* Paraptosis: a non-classical paradigm of cell death for cancer therapy. *Acta Pharmacol. Sin.* **45**, 223-237 (2024).
12. Fontana, F., Raimondi, M., Marzagalli, M., Di Domizio, A. & Limonta, P. The emerging role of paraptosis in tumor cell biology: Perspectives for cancer prevention and therapy with natural compounds. *BBA-Rev. Cancer* **1873**, 188338 (2020).
13. Lee, D., Kim, I.Y., Saha, S. & Choi, K.S. Paraptosis in the anti-cancer arsenal of natural products. *Pharmacol. Ther.* **162**, 120-133 (2016).
14. Bock, F.J. & Tait, S.W.G. Mitochondria as multifaceted regulators of cell death. *Nat. Rev. Mol. Cell. Biol.* **21**, 85-100 (2020).
15. Zhang, Y. *et al.* Mitochondria-targeted nanoparticles in treatment of neurodegenerative diseases. *Exploration* **1**, 20210115 (2021).
16. Wang, Y. *et al.* Small-molecule compounds target paraptosis to improve cancer therapy. *Biomed. Pharmacother.* **118**, 109203 (2019).
17. Zhao, L. *et al.* Nitrovin (difurazone), an antibacterial growth promoter, induces ROS-mediated paraptosis-like cell death by targeting thioredoxin reductase 1 (TrxR1). *Biochem. Pharmacol.* **210**, 115487 (2023).
18. Rajesh, Y. *et al.* Lumefantrine, an antimalarial drug, reverses radiation and temozolomide resistance in glioblastoma. *Proc. Natl. Acad. Sci. U. S. A.* **117**, 12324-12331 (2020).
19. Li, B. *et al.* Molecular Probe Crossing Blood–Brain Barrier for Bimodal Imaging–Guided Photothermal/Photodynamic Therapies of Intracranial Glioblastoma. *Adv. Funct. Mater.* **30**, 1909117 (2020).
20. Wang, L., Gundelach, J.H. & Bram, R.J. Cycloheximide promotes paraptosis induced by inhibition of cyclophilins in glioblastoma multiforme. *Cell Death Dis.* **8**, e2807-e2807 (2017).
21. Bury, M. *et al.* Ophiobolin A induces paraptosis-like cell death in human glioblastoma cells by decreasing BKCa channel activity. *Cell Death Dis.* **4**, e561-e561 (2013).
22. Zhou, Y. *et al.* Paraptosis-Inducing Nanomedicine Overcomes Cancer Drug Resistance for a Potent Cancer Therapy. *Small* **14**, 1702446 (2018).
23. Zheng, R.-R. *et al.* Paraptosis Inducer to Effectively Trigger Immunogenic Cell Death for Metastatic Tumor Immunotherapy with IDO Inhibition. *ACS Nano* **17**, 9972-9986 (2023).
24. Zheng, R. *et al.* Metal-coordinated nanomedicine for combined tumor therapy by inducing paraptosis and apoptosis. *J. Control. Release* **336**, 159-168 (2021).
25. Han, L. *et al.* Specific-oxygen-supply functionalized core-shell nanoparticles for smart mutual-promotion between photodynamic therapy and gambogic acid-induced chemotherapy. *Biomaterials* **257**, 120228 (2020).
26. Zeng, F. *et al.* Ferroptosis Detection: From Approaches to Applications. *Angew. Chem. Int. Ed.* **62**, e202300379 (2023).

27. Kang, N. *et al.* Stimuli-responsive ferroptosis for cancer therapy. *Chem. Soc. Rev.* **52**, 3955-3972 (2023).
28. Stockwell, B.R. Ferroptosis turns 10: Emerging mechanisms, physiological functions, and therapeutic applications. *Cell* **185**, 2401-2421 (2022).
29. Wu, C. *et al.* A nonferrous ferroptosis-like strategy for antioxidant inhibition–synergized nanocatalytic tumor therapeutics. *Sci. Adv.* **7**, eabj8833 (2021).
30. Jiang, Y. *et al.* Transformable hybrid semiconducting polymer nanozyme for second near-infrared photothermal ferrotherapy. *Nat. Commun.* **11**, 1857 (2020).
31. Lei, G., Zhuang, L. & Gan, B. Targeting ferroptosis as a vulnerability in cancer. *Nat. Rev. Cancer* **22**, 381-396 (2022).
32. Mei, J., Leung, N.L.C., Kwok, R.T.K., Lam, J.W.Y. & Tang, B.Z. Aggregation-Induced Emission: Together We Shine, United We Soar! *Chem. Rev.* **115**, 11718-11940 (2015).
33. Kenry & Liu, B. Enhancing the Theranostic Performance of Organic Photosensitizers with Aggregation-Induced Emission. *Acc. Mater. Res.* **3**, 721-734 (2022).
34. Liu, Z. *et al.* BSA-AIE Nanoparticles with Boosted ROS Generation for Immunogenic Cell Death Immunotherapy of Multiple Myeloma. *Adv. Mater.* **35**, 2208692 (2023).
35. Cen, P. *et al.* Aggregation-induced emission luminogens for in vivo molecular imaging and theranostics in cancer. *Aggregate* **4**, e352 (2023).
36. Wang, J. *et al.* A one-two punch targeting reactive oxygen species and fibril for rescuing Alzheimer's disease. *Nat. Commun.* **15**, 705 (2024).
37. Duo, Y. *et al.* Aggregation-induced emission: An illuminator in the brain. *Coordin. Chem. Rev.* **482**, 215070 (2023).
38. Zhang, T. *et al.* Near-Infrared Aggregation-Induced Emission Luminogens for In Vivo Theranostics of Alzheimer's Disease. *Angew. Chem. Int. Ed.* **62**, e202211550 (2023).
39. Zhang, J. *et al.* A Brain-Targeting NIR-II Ferroptosis System: Effective Visualization and Oncotherapy for Orthotopic Glioblastoma. *Adv. Sci.* **10**, 2206333 (2023).
40. Wu, M.-Y. *et al.* A near-infrared AIE fluorescent probe for myelin imaging: From sciatic nerve to the optically cleared brain tissue in 3D. *Proc. Natl. Acad. Sci. U.S.A.* **118**, e2106143118 (2021).
41. Wu, Q. *et al.* Janus luminogens with bended intramolecular charge transfer: Toward molecular transistor and brain imaging. *Matter* **4**, 3286-3300 (2021).
42. Fu, W. *et al.* Rational Design of Near-Infrared Aggregation-Induced-Emission-Active Probes: In Situ Mapping of Amyloid-β Plaques with Ultrasensitivity and High-Fidelity. *J. Am. Chem. Soc.* **141**, 3171-3177 (2019).
43. Pajouhesh, H. & Lenz, G.R. Medicinal chemical properties of successful central nervous system drugs. *NeuroRX* **2**, 541-553 (2005).
44. Ma, D. *et al.* Recent advances in the design and applications of near-infrared II responsive small molecule phototherapeutic agents. *Coordin. Chem. Rev.* **505**, 215677 (2024).
45. He, S., Cheng, P. & Pu, K. Activatable near-infrared probes for the detection of specific populations of tumour-infiltrating leukocytes in vivo and in urine. *Nat. Biomed. Eng.* **7**, 281-297 (2023).
46. Guo, X. *et al.* Mito-Bomb: Targeting Mitochondria for Cancer Therapy. *Adv. Mater.* **33**, 2007778 (2021).
47. Magut, P.K.S. *et al.* Tunable Cytotoxicity of Rhodamine 6G via Anion Variations. *J. Am. Chem. Soc.* **135**, 15873-15879 (2013).
48. Feng, H.-T., Yuan, Y.-X., Xiong, J.-B., Zheng, Y.-S. & Tang, B.Z. Macrocycles and cages based on tetraphenylethylene with aggregation-induced emission effect. *Chem. Soc. Rev.* **47**, 7452-7476 (2018).
49. Zeng, S. *et al.* Fluorescent dyes based on rhodamine derivatives for bioimaging and therapeutics: recent progress, challenges, and prospects. *Chem. Soc. Rev.* **52**, 5607-5651 (2023).
50. Cao, S. *et al.* Solvatochromic Near-Infrared Aggregation-Induced Emission-Active Acrylonitriles by Acceptor Modulation for Low-Power Stimulated Emission Depletion Nanoscopy. *Chem. Mater.* **35**, 2472-2485 (2023).
51. Gandin, V. *et al.* In Vitro and in Vivo Anticancer Activity of Copper(I) Complexes with Homoscorpionate Tridentate Tris(pyrazolyl)borate and Auxiliary Monodentate Phosphine Ligands. *J. Med. Chem.* **57**, 4745-4760 (2014).
52. Sperandio, S. *et al.* Paraptosis: mediation by MAP kinases and inhibition by AIP-1/Alix. *Cell Death Differ.* **11**, 1066-1075 (2004).
53. Raimondi, M. *et al.* Ca2+ overload- and ROS-associated mitochondrial dysfunction contributes to δ-tocotrienol-mediated paraptosis in melanoma cells. *Apoptosis* **26**, 277-292 (2021).
54. Kuang, S. *et al.* Photodecaging of a Mitochondria-Localized Iridium(III) Endoperoxide Complex for Two-Photon Photoactivated Therapy under Hypoxia. *J. Am. Chem. Soc.* **144**, 4091-4101 (2022).
55. Chen, D. *et al.* iPLA2β-mediated lipid detoxification controls p53-driven ferroptosis independent of GPX4. *Nat. Commun.* **12**, 3644 (2021).
56. Kroemer, G. *et al.* Classification of cell death: recommendations of the Nomenclature Committee on Cell Death 2009. *Cell Death Differ.* **16**, 3-11 (2009).
57. Fang, X. *et al.* Ferroptosis as a target for protection against cardiomyopathy. *Proc. Natl. Acad. Sci. U.S.A.* **116**, 2672-2680 (2019).
58. Cheng, T. *et al.* Computation of Octanol−Water Partition Coefficients by Guiding an Additive Model with Knowledge. *J. Chem. Inf. Model.* **47**, 2140-2148 (2007).
59. Hitchcock, S.A. & Pennington, L.D. Structure−Brain Exposure Relationships. *J. Med. Chem.* **49**, 7559-7583 (2006).

Acknowledgements

This work was supported by the National Natural Science Foundation of China (62105184, 22275050, 32071388, 22205096, and 51620105009), the Joint Training Funds for Science & Technology R&D of Henan Province (222301420059), the Program for Science & Technology Innovation Talents in Universities of Henan Province (22HASTIT004), the Shenzhen Key Laboratory of Functional Aggregate Materials (ZDSYS20211021111400001), the

Innovation and Technology Commission (ITC-CNERC14SC01 and ITCPD/17-9), and the Teli Young Scholar Program of Beijing Institute of Technology.

Author contributions

J.W. and G.N. supervised the work. B.S. and B.Z.T. conceived the idea for this work. M.C. synthesized the materials, measured the photophysical data, and performed the calculation. L.H., P.S., Y.L., and Y.Z. performed the cell and animal assays. C.C. and H.H.Y.S. contributed to the materials preparation and crystal determination. G.W., X.C., and M.L. assisted in the cell toxicity and imaging characterizations. M. L., Z.L., M. H., and J.W.Y.L. assisted the in vivo imaging assays. J.W., G.N., B.S., and B.Z.T. analyzed the data and wrote the manuscript. All the authors contributed to the interpretation of the data and preparation of the manuscript.

Competing interests

The authors declare no competing interests.